

On the Use of Multipolarization Satellite SAR Data for Coastline Extraction in Harsh Coastal Environments: The Case of Solway Firth

Emanuele Ferrentino¹, Student Member, IEEE, Andrea Buono², Member, IEEE, Ferdinando Nunziata³, Senior Member, IEEE, Armando Marino⁴, Member, IEEE, and Maurizio Migliaccio⁵, Fellow, IEEE

Abstract—This study deals with coastline extraction using multipolarization spaceborne synthetic aperture radar (SAR) imagery acquired over coastal intertidal areas. The latter are very challenging environments where mud flats lead to a large variability of normalized radar cross section, which may trigger a significant number of false edges during the extraction process. The performance of SAR-based coastline extraction methods that rely on a joint combination of multipolarization information (either single- or dual-polarization metrics) and speckle filtering (either local and nonlocal approaches) are analyzed using global positioning system (GPS) samples and colocated SAR imagery collected under different incidence angles. Our test site is an intertidal zone with a wetland (i.e., salt marsh) in the Solway Firth, south-west along the Scottish-English border. Experimental results, obtained processing a pair of RadarSAT-2 full-polarimetric and a pair of Sentinel-1 dual-polarimetric SAR imagery augmented by colocated GPS samples, show that: first, the multipolarization information outperforms the single-polarization counterpart in terms of extraction accuracy; second, among the single-polarization channels, the cross-polarized one performs best; third, both single- and dual-polarization methods perform better when nonlocal speckle filtering is applied; fourth, the joint combination of nonlocal speckle filter and dual-polarization information provides the best accuracy; and finally, the incidence angle plays a role in the extraction accuracy with larger incidence angles resulting in the best performance when dual-polarization metric is used.

Index Terms—Coastal areas, coastline extraction, polarization, solway firth, synthetic aperture radar (SAR).

Manuscript received May 20, 2020; revised September 24, 2020 and October 28, 2020; accepted November 3, 2020. Date of publication November 6, 2020; date of current version January 6, 2021. This work was supported in part by the European Space Agency (ESA) under the ESA-MOST (Chinese Ministry of Science and Technology) Dragon-5 Cooperation Project ID 57 979 entitled “Monitoring Harsh Coastal Environments and Ocean Surveillance Using Radar Remote Sensing.” (Corresponding author: Maurizio Migliaccio.)

Emanuele Ferrentino, Andrea Buono, and Ferdinando Nunziata are with the Dipartimento di Ingegneria, Università degli Studi di Napoli Parthenope, 80133 Napoli, Italy (e-mail: emanuele.ferrentino@uniparthenope.it; andrea.buono@uniparthenope.it; ferdinando.nunziata@uniparthenope.it).

Armando Marino is with the Faculty of Natural Sciences, University of Stirling, FK9 4LA Stirling, U.K. (e-mail: armando.marino@stir.ac.uk).

Maurizio Migliaccio is with the Dipartimento di Ingegneria, Università degli Studi di Napoli Parthenope, 80133 Napoli, Italy, and also with the Istituto Nazionale di Geofisica e Vulcanologia, 00143 Rome, Italy (e-mail: mnm.migliaccio@gmail.com).

Digital Object Identifier 10.1109/JSTARS.2020.3036458

I. INTRODUCTION

COASTAL areas represent key economic assets, with high-density urban settlements and significant biodiversity heritage. Nonetheless, those areas are often strongly affected by extreme meteo-marine conditions and erosion processes, which threaten the stability of land and the safety of people. Observing the coastline from space in a continuous and effective way is of paramount importance to support coastal zone planning and management [1].

The synthetic aperture radar (SAR) is an imaging radar that provides systematic acquisitions characterized by all-day and almost all-weather meter-level spatial resolution and dense enough revisit time. Within the context of monitoring intertidal areas, SAR represents a key player. Nevertheless, SAR images are speckled, which means they are affected by a multiplicative noise that severely hampers the image interpretability and affects the accuracy of coastline extraction. Typically, multilooking procedures based on local averages are exploited to reduce speckle noise at the expense of spatial resolution [2]. In addition, the lack of land/sea contrast is also a key issue that limits the coastline extraction capabilities. Those issues are even worse when dealing with challenging coastal environments that call for inaccurate estimates of normalized radar cross section (NRCS) over the land/sea boundary.

In this study, a comparison of coastline extraction methodologies is presented that aims at evaluating the performance over a selected test site showing a very challenging coastal environment, i.e., the intertidal areas and salt marshes of the Solway Firth (Scotland). The comparison will test different combinations of multipolarization SAR metrics and both local and nonlocal speckle filters.

The majority of shoreline extraction studies apply image processing techniques and edge detection on single-polarization multilooked SAR imagery. Then, the extracted coastline profile is contrasted with the visually inspected coastline to qualitatively discuss the accuracy of the proposed technique [3], [4]. The extraction of the coastline is addressed using multipolarization SAR imagery in [5] and [6] using image anisotropic diffusion and spectral-textural segmentation. Again, the comparison is performed using a manually extracted reference coastline. In [7], the accuracy of the coastline extracted over the coast of Gabon

is discussed against the incidence angle. Results show that the cross-polarization channel provides the best performance at lower incidence angles $< 30^\circ$ while no polarization dependence is observed at larger incidence angles ($> 30^\circ$). In [8] and [9], the accuracy of the extracted coastline is discussed against the SAR frequency, showing that higher frequencies (C and X bands) perform best.

The coastline extracted using multipolarimetric SAR imagery is contrasted with ground-based information obtained using global positioning system (GPS) in [10] and [11]. The extraction accuracy is lower than 4 pixels in [10] when X-band dual-polarimetric Ping Pong (HH+VV) COSMO-SkyMed SAR imagery collected in the muddy sand intertidal flat area of Lingang New City, China are used. The average accuracy is up to 4.6 pixels in [12] when multipolarization C- and X-band SAR imagery collected over Monasterace, Italy, are used. The accuracy is up to 4 pixels in [11] when full-polarimetric C-band RadarSAT-2 SAR imagery collected over sandy beaches in Italy are processed. All the abovementioned studies rely on the use of SAR imagery where the speckle was filtered using conventional local approaches.

In recent years, nonlocal filters have been exploited to reduce speckle noise in SAR imagery while preserving fine spatial details [13], [14]. To the best of authors' knowledge, there is only one study that explicitly addressed the use of nonlocal speckle filters for coastline extraction purposes [15], where single-polarization X-band TanDEM-X pursuit monostatic SAR measurements were considered. Experiments, undertaken on a sandy/rocky coast along the English Channel and a skerry coast over Stockholm (Sweden), suggest that the use of nonlocal speckle filters can improve the extraction accuracy, (evaluated with respect to manually traced reference coastline), from 1 pixel up to 4 pixels, depending on the complexity of the coastal environment.

This study aims at analyzing the capability of SAR-based coastline extraction in challenging intertidal areas. The ability of polarimetric SAR (polSAR) measurements to provide reliable information on the tidal flats has been demonstrated in several studies (e.g., [8], [16]–[19]). Hence, here we aim at advancing these studies by quantitatively discussing the performance of the multipolarization coastline extraction methods over a challenging intertidal zone. On this purpose, an experimental campaign where we collected GPS samples spatially and timely collocated with full-polarimetric RadarSAT-2 SAR overpasses was conducted over the Solway Firth coastal area. This latter is a special area of conservation whose coastal profile is characterized by an almost open, wind-swept, dynamic and tidal landscape that includes different habitats as wetland, salt marshes, sand dunes, and mudflats [20]. Accordingly, the selected test area represents an ideal test case for the purposes of this study. The main contributions and the goals of this study are: first, to address the capability of polSAR to extract the coastline related to intertidal areas; second, to quantitatively assess the coastline extraction performance of multipolarization metrics; third, to quantitatively evaluate the contribution of dual-polarization information and nonlocal speckle filters with respect to single-polarization NRCS and conventional local filters; and final, to quantitatively

discuss the effect of incidence angle on the coastline extraction accuracy by means of additional dual-polarimetric Sentinel-1 SAR data.

The remainder of the article is organized as follows: the methodology is presented in Section II; whereas the test site is described in Section III. The dataset is presented in Section IV, whereas experiments are discussed in Section V. The Conclusion is drawn in Section VI.

II. METHODOLOGY

The methodology adopted to extract the coastline from multipolarization SAR satellite data consists of the following steps.

- 1) Radiometric calibration, to obtain the NRCS values from the digital numbers.
- 2) Speckle filtering, to reduce the multiplicative noise from the NRCS image.
- 3) Metric evaluation, to evaluate the single- and the dual-polarization features.
- 4) Land/sea binary image generation, by applying a global threshold constant false alarm rate (CFAR) to the output of the metric.
- 5) Morphological filtering, to refine the binary image by removing artifacts and filling holes.
- 6) Edge detection, to extract the continuous coastline from the refined binary image.
- 7) Geocoding, to project the extracted coastline on a geographic reference system.
- 8) Performance assessment, by comparing the extracted coastline with collocated GPS samples.

The complete flowchart of the processing chain is depicted in Fig. 1. For the purpose of this study, speckle filtering, metric evaluation, land/sea binary image generation, and edge detection are hereinafter fully discussed. Additional information on the other processing steps can be found in [12], [21], and [22].

Speckle filtering aims at reducing the speckle noise to improve the observation of the land/sea boundary while ideally preserving the edge information. Since speckle filtering results in spatial resolution loss, a tradeoff between noise reduction, edge preservation and satisfactory resolution must be achieved. In literature, multilooking and local filters, i.e., filters that involve spatial averaging of neighboring pixels, are usually adopted for speckle reduction to extract the coastline from SAR imagery [5], [12], [23]–[25]. The most used speckle filters are the boxcar and Lee filter. The former consists of an incoherent averaging of neighboring pixels within an $N \times N$ sliding window, while the latter consists of using an adaptive filtering coefficient that depends on the local statistics [2].

Recently, speckle filtering based on nonlocal paradigms is suggested as a way to optimize noise reduction and edge preservation [15]. Nonlocal filters exploit the significant level of redundancy within a SAR image, i.e., similar patches characterized by the same intensity/scattering features are widely present in the same SAR image. Hence, the underpinning idea is to consider, in the filtering process, “similar” pixels selected and weighted according to some patch-based similarity criteria [26]. Accordingly, a smaller patch window and a larger search window

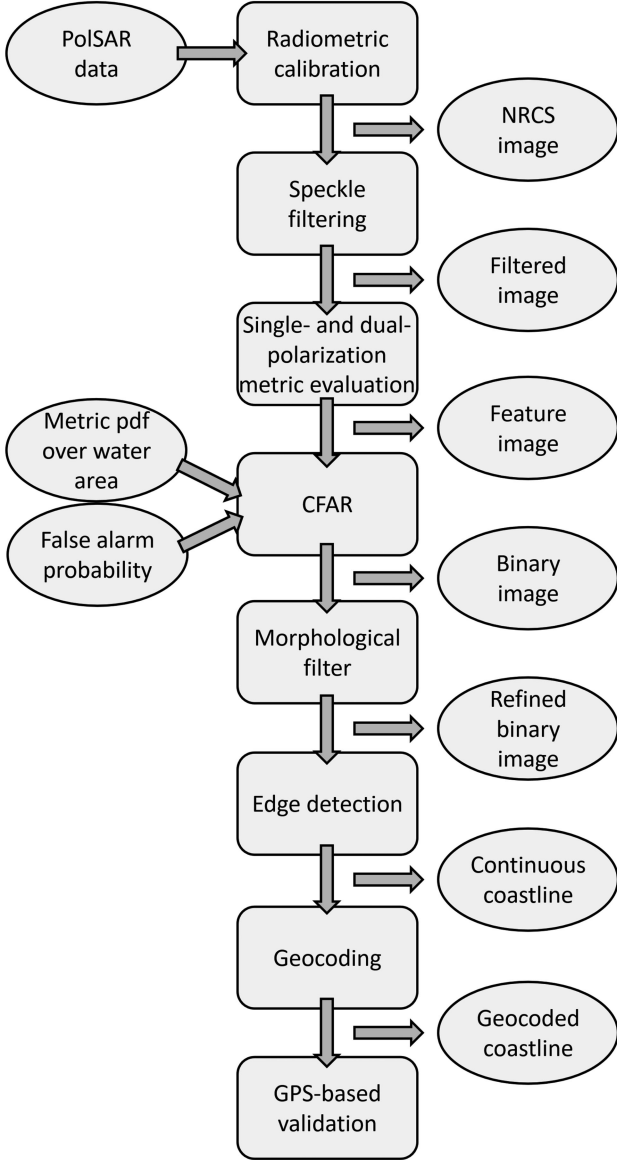


Fig. 1. Flowchart of the coastline extraction methodology. Input (outputs) are placed on the right (left) side, while processing steps lie in the center.

must be set. This nonlocal filtering approach was found to provide remarkable speckle reduction capabilities while keeping fine edges, which is highly desired for coastline extraction purposes [15]. Hence, it is worth expecting that nonlocal filtering improves the accuracy of the extracted coastlines over areas calling for a large variability of NRCS. In fact, the selection along with the whole SAR image of patches calling for similar scattering behavior is expected to reduce the speckle noise while preserving a remarkable level of details to guarantee a more accurate, i.e., with a smaller bias and a limited number of false edges, coastline extraction process. Several nonlocal speckle filtering approaches have been proposed that deal with different SAR data (single-polarization, polarimetric, interferometric, polInSAR) and similarity criteria (sum of the squared difference, generalized likelihood ratio, logarithm of the arithmetic versus

geometric mean ratio, Kullback–Leibler distance, etc.). Further details can be found in [26]. In this study, the nonlocal mean approach originally proposed in [27] and [28] is adopted.

The metric evaluation consists of selecting a suitable parameter from which the coastline can be extracted in a robust and effective way. When dealing with single-polarization SAR measurements, the NRCS is exploited; when dealing with dual-polarization SAR measurements, the product of co- and cross-polarized amplitude channels is exploited. Hence, in this study, the capability of the following metrics is investigated:

$$\sigma_{xx}^0 = \langle |S_{xx}|^2 \rangle, \quad \sigma_{xy}^0 = \langle |S_{xy}|^2 \rangle \quad (1)$$

$$r_{xx+xy} = \langle |S_{xx}| \cdot |S_{xy}| \rangle \quad (2)$$

where $\{x, y\} \in \{H, V\}$, $|\cdot|$ and $\langle \cdot \rangle$ stand for modulus and spatial averaging, respectively.

The generation of the binary image is obtained by processing the output of the metric with a CFAR approach based on the statistical distribution of the clutter. In [21], it was shown that, under low-to-moderate wind conditions and intermediate incidence angles, the empirical statistical distribution of NRCS and r over a reference sea area is well-approximated by the generalized Gamma and the Burr distribution, respectively. Accordingly, given the relationship between the probability of false alarm P_{fa} and the CFAR global threshold th , the latter can be obtained according to (3) and (4) for NRCS and r metrics, respectively, where α , μ , and β are the nonnegative shape and scale parameters of the generalized Gamma distribution; while σ and η are the nonnegative scale and power parameters, ν is the shape parameter and $\Gamma(\cdot)$ is the Gamma function [21].

$$th_{\sigma^0} = \left(\beta \left[P_{fa}^{-\frac{1}{\alpha}} - 1 \right] \right)^{\frac{1}{\mu}} \quad (3)$$

$$th_r = \begin{cases} \sigma \left(\frac{1}{\eta} \Gamma^{-1} (1 - P_{fa}, \eta) \right)^{\frac{1}{\nu}}, & \nu > 0 \\ \sigma \left(\frac{1}{\eta} \Gamma^{-1} (P_{fa}, \eta) \right)^{\frac{1}{\nu}}, & \nu < 0 \end{cases} \quad (4)$$

In this study, P_{fa} is always set to 10^{-6} since it was experimentally found to result in the best performance in terms of false edges while calling for a limited number of false coastlines.

The edge detection consists of extracting the 1-pixel continuous coastline using an edge detector algorithm applied to the binary image. In this study, the optimal Canny edge detector, which is based on a 2-D Gaussian kernel that allows emphasizing edges, is used [29].

III. TEST SITE

The selected test site consists of the inner part of the Solway Firth, that includes the eastern bank of the river Nith estuary (termed as Caerlaverock) a large embayment located in the south-western Scotland coast, in the north-eastern Irish Sea, between the Scottish region Dumfries and Galloway and the English area of Cumbria (see Fig. 2). It is one of the largest estuarine systems in the United Kingdom.

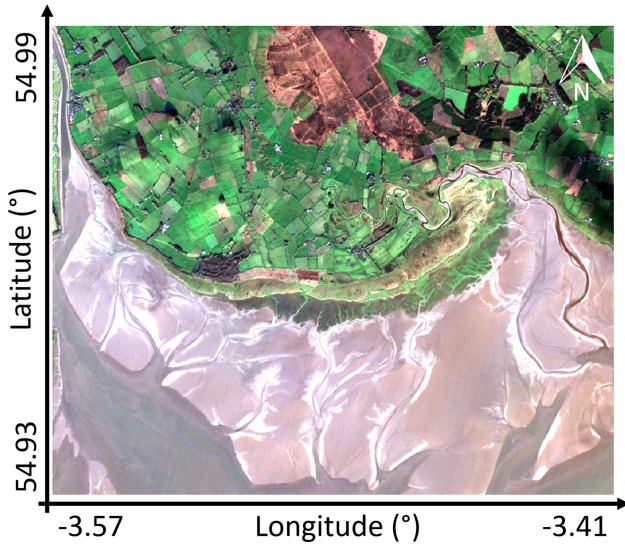


Fig. 2. True color optical image, relevant to a Sentinel-2 MSI acquisition collected over the test area of Caerlaverock, Solway Firth, on November 26, 2018.

The Solway Firth was designated as an “Area of Outstanding Natural Beauty” due to its wonderful landscape since 1964 and, nowadays, it hosts about 300 km² of sites of special scientific interest. The Solway Firth was also declared a marine special area of conservation due to its richness in biodiversity. In addition, the Robin Rigg offshore wind farm is just 20 km off the Solway Firth coast.

The coastal area of the Solway Firth is mainly characterized by drained lowland hills and small mountains within 0.5 km of the actual coastline, while toward the sea it calls for large wetland areas that consist of salt marshes and mudflats [30]. In particular, mudflats often contain dangerous patches of quicksand that move frequently. A large amount of river-induced intertidal salt marsh sediments and fine-grained mudflat are also present, which are partly characterized by significant concentration of caesium 137 radionuclides due to the contaminating Sellafield nuclear fuel reprocessing plant.

The Solway Firth bathymetry is characterized by shallow water and is influenced by the macrotidal range associated to the river estuary that induces significant movements of sand and silt [30]. The macrotidal range is about 7 m on average but, depending on the season, the tidal range can reach up to 9 m. As a result, there are large areas (in the order of several km) characterized by intertidal sandbanks, mudflats, and marshes, exposed at low tide [31]. The lower marsh over the mudflats, whose width goes from 30 m up to 220 m during the year, is completely emerged most of the times during spring tides. With reference to the Caerlaverock test area, the tide-time of Caerlaverock is about 1 h-delayed with respect to the closest tide gauge, located in Southernness (about 11 km downstream of the Solway Firth) due to the slow water motion over the mudflats. Hence, the extremely variable mudflat microtopography that characterizes the test site prevents any accurate knowledge of the waterline at the time of SAR acquisitions. Nonetheless, in both the SAR scenes the Southernness tide was near the lowest

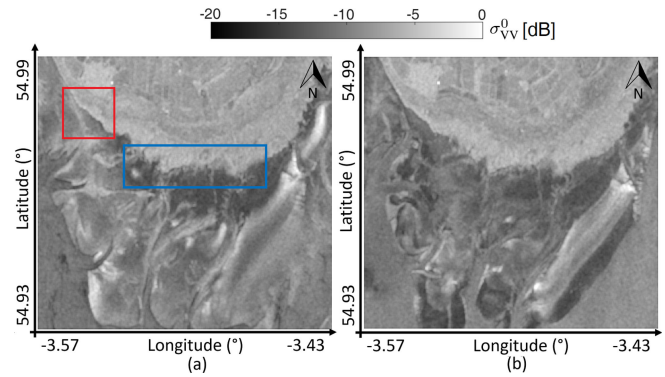


Fig. 3. Excerpt of RadarSAT-2 VV-polarized NRCS SAR images, in graytones and dB scale, collected over the test area of Caerlaverock, Solway Firth. (a) May 13, 2019. (b) July 5, 2018. The areas where qualitative (blue box) and quantitative (red box) analysis are performed are also annotated.

extreme and, therefore, a large part of the mud area is not water covered.

The Caerlaverock area is severely affected by coastal erosion, even induced by storm surges during the rainy winter season, that produce coastal terraces up to 1-m high. Nevertheless, it was found that more than 1000 ha of new marsh has developed in the Solway Firth since 1850, with the largest expansion (by a factor 6) occurred just in front of Caerlaverock [31]. This kind of coastal habitat can protect the coastline from erosion and provide highly effective long-term carbon storage potential. Hence, the Solway Firth coastal ecosystem needs to be preserved even to provide a long-term sink for atmospheric carbon dioxide.

IV. DATASET

In this section, the dataset, which includes both SAR and collocated GPS measurements, is presented. The dataset consists of two SAR scenes and GPS samples collected during *in-situ* campaigns concurrent with the SAR acquisitions time. For the purpose of this study, a controlled experiment was undertaken where a ground survey that aimed at collecting GPS samples was performed. In addition, timely and spatially collocated RadarSAT-2 overpasses were acquired.

The SAR imagery were collected over the Solway Firth area by the Canadian RadarSAT-2 spaceborne SAR sensor on July 5, 2018 and May 13, 2019 at 17:58 UTC (Coordinated Universal Time), see Fig. 3(a) and (b), respectively. Both SAR scenes were acquired at C-band (5.405 GHz), in ascending pass and in fine full-polarimetric imaging mode, with an incidence angle of 38° at mid-range. The SAR scenes are processed to obtain a pixel spacing of 5 m. To discuss the performance of coastline extraction against the incidence angle, two SAR scenes were collected from the European Sentinel-1 satellites on July 1 and 2, 2018, at 17:58 UTC. Both SAR scenes were acquired at C-band, in ascending pass and in dual-polarimetric VV+VH Interferometric Wide (IW) imaging mode, with an incidence angle of 38° and 45°, respectively. The SAR scenes are processed to obtain a pixel spacing of 13 m.

The GPS dataset consists of 29 samples collected on July 5, 2018 and 89 samples gathered on May 13, 2019. During

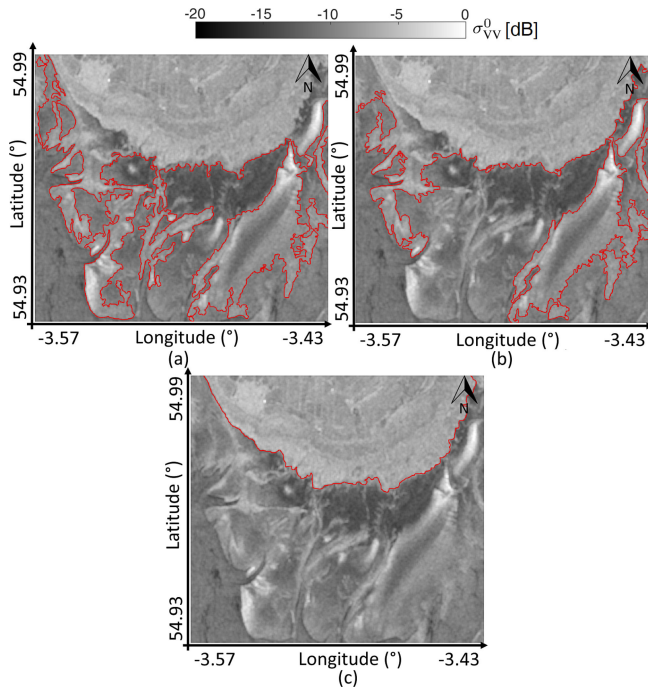


Fig. 4. Coastline extracted. (a) σ_{HH}^0 . (b) σ_{VV}^0 . (c) σ_{VH}^0 superimposed as a red line onto the σ_{VV}^0 image of Fig. 3(a).

the *in-situ* campaign, a commercial Garmin model “72H” GPS operating in United States Coast Guard Differential GPS (USCG DGPS) mode was used that achieves a positioning accuracy in the range 3–5 m with ± 1 m uncertainty. Hence, considering the RadarSAT-2 SAR spatial resolution, the localization capability of the GPS samples is at the pixel level.

V. EXPERIMENTS

In this section, the coastline is extracted using multipolarization SAR scenes collected over the Solway Firth area before and after the 2019 storm season, see Fig. 3(a) and (b), respectively. According to the methodology described in Section II, different multipolarization metrics [see (2)] are used to extract the coastline along with either local and nonlocal filters. For each speckle filter, the windows’ size that provides the best coastline extraction accuracy is selected. The extracted coastline is verified against GPS samples.

The first experiment consists of processing the SAR scene of Fig. 3(a) using single-polarization metrics. The scene is very challenging in terms of coastline extraction due to the large NRCS variability that results from the intertidal area. This variability is expected to call for a large number of false edges over the wetland area. The coastlines extracted from the σ_{HH}^0 , σ_{VV}^0 , and σ_{VH}^0 imagery using a 9×9 boxcar filter are depicted in Fig. 4 (a)–(c), respectively. The coastlines are superimposed as red lines onto the σ_{VV}^0 image of Fig. 3(a). By visually inspecting the extracted coastline, it can be noted that copolarized channels do not provide satisfactory accuracy since they result in coastlines calling for large departures from the actual profile. In addition, a large number of false edges are visible in the intertidal area.

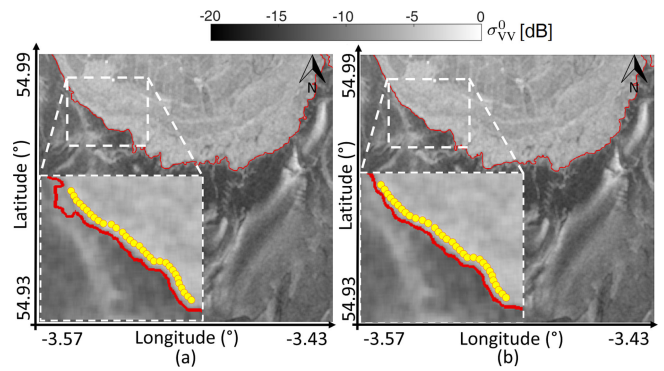


Fig. 5. Coastline extracted. (a) r_{HH+HV} . (b) r_{VV+VH} superimposed as red lines onto the σ_{VV}^0 imagery of Fig. 3(a). An enlarged version of the area that includes GPS samples (yellow dots) is also shown in the annotated inset.

The worst performance is achieved by the σ_{HH}^0 metric that results in the largest NRCS variability over the intertidal area. This is inherently due to the morphological features of the test area that calls for large sand banks and wetlands together with sediments coming from the river Nith that make the off-shore environment very challenging. A remarkable visual agreement with the coastal profile is obtained when using the σ_{VH}^0 metric, see Fig. 4 (c). This means that the cross-polarized channel results in the lowest NRCS variability within the intertidal area. In fact, in this case, no false edge is detected.

The second experiment consists of processing the SAR scene of Fig. 3(a) using the dual-polarization metrics r_{HH+HV} and r_{VV+VH} [see (2)] and a 9×9 boxcar filter, see Fig. 5 (a) and (b), respectively, where the extracted coastline is superimposed as a red line onto the σ_{VV}^0 image of Fig. 3(a). By visually inspecting the extracted coastline, no remarkable difference appears since they both call for a good match with the visually inspected coastal profile and none of them results in false edges in the off-shore area. To quantitatively analyze the performance of the two metrics, the reference ground-based GPS information is used. The yellow dots in the inset highlighted in Fig. 5 show the GPS samples. Although both the extracted coastlines well-fit the actual profile, larger departures are achieved by the r_{HH+HV} metric, in particular in the north-western part of the area. This odd result can be explained with the larger sensitivity of the σ_{HH}^0 channel to the very heterogeneous intertidal area that results in a worsening of the r_{HH+HV} performance with respect to the r_{VV+VH} metric.

In the subsequent experiments, we focus on the σ_{VH}^0 and r_{VV+VH} (hereinafter r) metrics since they resulted in the best accuracy and robustness against false edges.

The third experiment aims at intercomparing the performance of the coastline extracted from σ_{VH}^0 and r using different filtering methods. The coastlines related to the SAR scene of Fig. 3(a) extracted from σ_{VH}^0 and r using both local and nonlocal speckle filters are depicted in Fig. 6 (a) and (b), respectively. They are superimposed onto the geocoded true color Sentinel-2 multispectral instrument (MSI) image collected over the test area during the same date of the SAR acquisition of Fig. 3(a). The extracted coastlines that refer to the local boxcar and Lee speckle

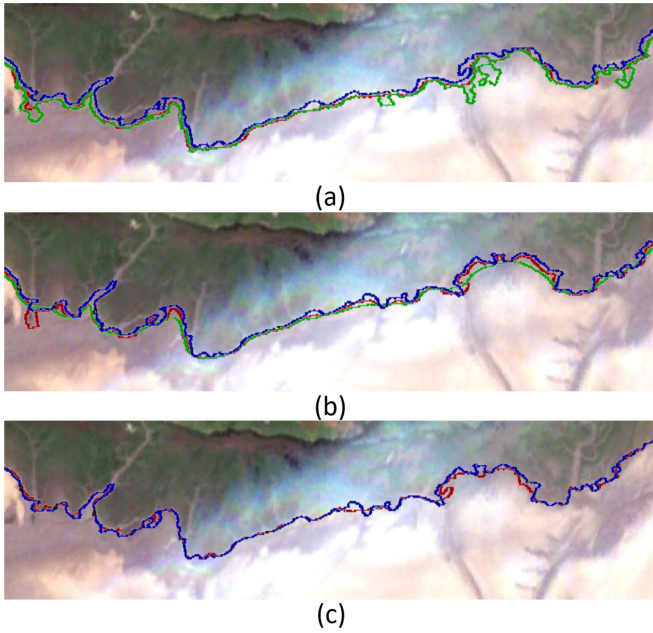


Fig. 6. Coastlines extracted. (a) σ_{VH}^0 . (b) r related to the area marked by the blue box in Fig. 3(a) and superimposed onto the collocated Sentinel-2 MSI true color image. The coastlines extracted using the boxcar and Lee filters and the nonlocal filter are depicted as red, green, and blue lines, respectively. The coastlines extracted from r (blue line) and σ_{VH}^0 (red line) using the nonlocal filter are shown in (c).

filters are depicted as red and green lines, respectively, while the nonlocal one is shown as a blue line. By visually analyzing the extracted coastlines, one can note that neither σ_{VH}^0 nor r result in false edges in the intertidal area. When dealing with the extraction accuracy, local filters result in the worst performance, with the boxcar filter and the Lee filter resulting in the largest departure from the visually inspected coastal profile in the r and σ_{VH}^0 metrics, respectively. The coastlines extracted from r and σ_{VH}^0 using the nonlocal filter are visually intercompared in Fig. 6, (c) where the two coastlines are depicted as blue and red lines, respectively. It can be noted that the two coastlines exhibit a fair enough overlapping in the western part of the scene, while they call for larger departure in the eastern area of the image.

To quantitatively analyze the performance of the extracted coastlines, ground-based GPS samples are used. The coastlines extracted using boxcar (red line), Lee (green line), and nonlocal (blue line) speckle filters are depicted in Fig. 7 where σ_{VV}^0 is used as the reference background image. Note that for both local filters a 9×9 window size is used, whereas for the nonlocal filter the search and patch windows' size has been set to 21×21 and 7×7 , respectively, as suggested in [15]. Fig. 7 is organized in a matrix format where the rows refer to the coastlines extracted using σ_{VH}^0 and r metrics; while the columns refer to the SAR scenes of Fig. 3.

By visually inspecting the extracted coastlines, it can be noted that the profiles extracted from the scene of Fig. 3(a) are noisier than the ones related to the scene of Fig. 3(b). This witnesses that the storm season made the coastal area more challenging in terms of coastline extraction. In addition, the coastlines extracted from r appear less noisy than the σ_{VH}^0 ones. In fact, the σ_{VH}^0

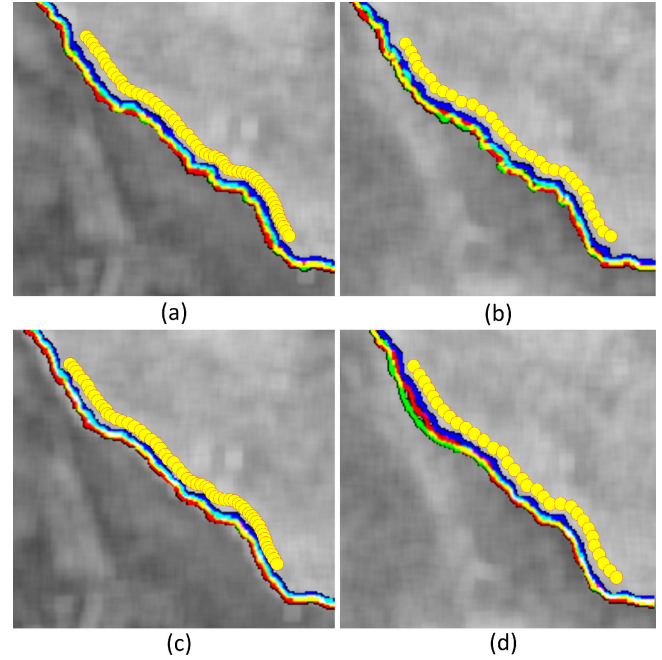


Fig. 7. Coastline extracted from σ_{VH}^0 related to the SAR scene. (a) Fig. 3(a). (b) Fig. 3(b). The coastline extracted from r related to the SAR scene. (c) Fig. 3(a). (d) Fig. 3(b). The coastlines, superimposed on the corresponding σ_{VV}^0 image, are coded as red, green, and blue lines for the boxcar, Lee and nonlocal speckle filter, respectively. GPS samples are annotated as yellow dots.

metric results in coastlines that exhibit deviation with respect to the profile identified by the GPS samples when the local filters are used. Nonetheless, those fluctuations are flattened out by the nonlocal filter. The coastlines extracted from r do not exhibit significant fluctuations. However, departures from the GPS-based coastline appear when the local filters are used.

To quantify the accuracy of the extracted coastlines, the distance in pixels between the GPS samples timely collocated with the SAR scene of Fig. 3(a) and the corresponding points belonging to the extracted coastlines is evaluated and depicted in Fig. 8.

It can be noted that, when local speckle filters are used, the coastline extracted from r always outperforms the σ_{VH}^0 one. When the nonlocal filter is used r outperforms σ_{VH}^0 in the 60% of cases. When a threshold equal to 5 pixels is set, this accuracy is never achieved when the boxcar filter is used; while it is met in just the 2% of cases when the Lee filter is used. The performance improves significantly when the nonlocal filter is used, which meets the threshold accuracy in the 25% and 21% of cases for r and σ_{VH}^0 , respectively. When the threshold is relaxed to 6 pixels, the boxcar filter still does not meet the requested accuracy. The Lee filter meets the threshold accuracy just in the 6% (r) and 4% (σ_{VH}^0) of cases. Again, the best result is provided by the nonlocal filter, whose performance meets the threshold accuracy in the 53% (r) and 58% (σ_{VH}^0) of cases. This is due to the fact that, as suggested in [15], the nonlocal filters, by exploiting the scattering similarity between patches through the whole SAR image, provide better performance in preserving spatial details while reducing speckle noise with respect to local

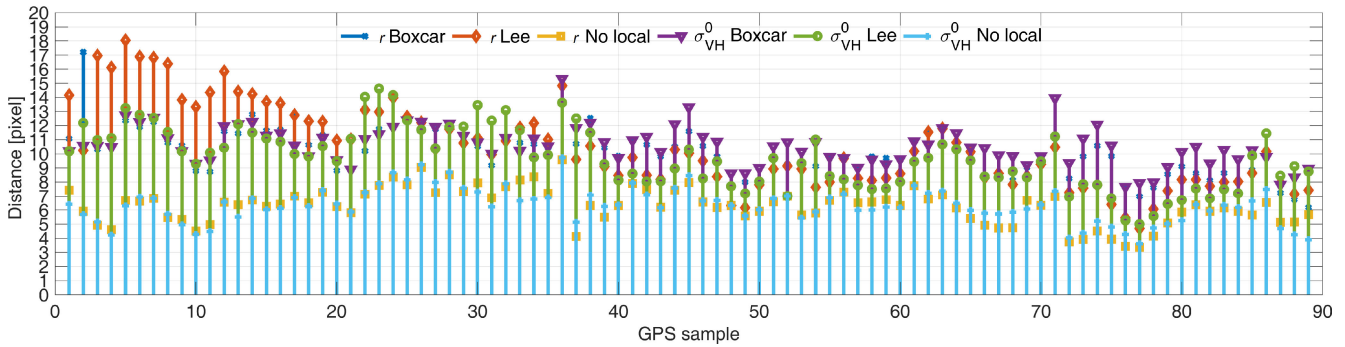


Fig. 8. Distance in pixels between the GPS samples timely collocated with the SAR scene of Fig. 3(a) and the corresponding points belonging to the coastlines extracted from r and σ_{VH}^0 metrics using different speckle filters.

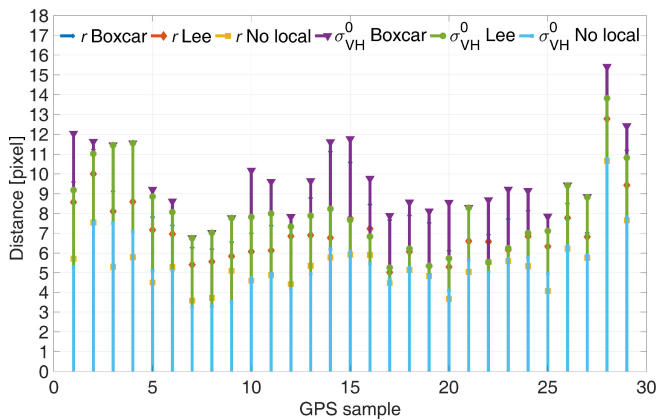


Fig. 9. Distance in pixels between the GPS samples timely collocated with the SAR scene of Fig. 3(b) and the corresponding points belonging to the coastlines extracted using r and σ_{VH}^0 metrics using different speckle filters.

filters, especially in heterogeneous areas characterized by large NRCS variability.

The same exercise is undertaken on the plot of Fig. 9, which is related to the SAR scene of Fig. 3(b). Once again, when local filters are used, the coastline extracted from r always outperforms the σ_{VH}^0 one. When the nonlocal filter is used r outperforms σ_{VH}^0 in the 65% of the cases. When a threshold equal to 5 pixels is set, this accuracy is never achieved by the boxcar filter; while it is met in the 10% of cases by the Lee filter. The performance significantly improves when the nonlocal filter is used, which meets the threshold accuracy in the 60% of cases for both r and σ_{VH}^0 . When the threshold is relaxed to 6 pixels, the boxcar filter still does not meet the requested accuracy when the σ_{VH}^0 metric is adopted; while reaching the threshold accuracy in the 10% of cases when r is used. The Lee filter meets the requested accuracy in the 38% (r) and 21% (σ_{VH}^0) of cases. Again, the best accuracy is obtained by the nonlocal filter, whose performance meets the threshold in the 90% (r) and 83% (σ_{VH}^0) of cases. This result can be explained by the capability of nonlocal filters to enhance the land-to-water separability by both reducing the land outliers and the water clutter [15].

TABLE I
MEAN AND STANDARD DEVIATION DISTANCE (PIXELS) BETWEEN GPS MEASUREMENTS AND THE CORRESPONDING POINTS BELONGING TO THE COASTLINE EXTRACTED USING r AND σ_{VH}^0

| Scene | Metric | Speckle filter | | | | | |
|------------|-----------------|----------------|-----|------|-----|-----------|-----|
| | | Boxcar | | Lee | | Non-local | |
| | | Mean | Std | Mean | Std | Mean | Std |
| Fig. 3 (a) | r | 10.2 | 1.8 | 10.4 | 2.9 | 6.3 | 1.3 |
| | σ_{VH}^0 | 10.6 | 1.4 | 9.7 | 2.1 | 6.3 | 1.2 |
| Fig. 3 (b) | r | 8.3 | 1.8 | 7.1 | 1.6 | 5.4 | 1.4 |
| | σ_{VH}^0 | 9.6 | 1.9 | 8.2 | 2.1 | 5.6 | 1.5 |

The mean accuracy measured in terms of mean \pm standard deviation distance (in pixels) with respect to GPS samples is listed in Table I.

When dealing with the SAR scene of Fig. 3(a), the best average accuracy (6.3 pixels) results from the joint combination of either r and σ_{VH}^0 with the nonlocal speckle filter. Those combinations are also the most robust, with a standard deviation lower than 1.4 pixels. The use of local speckle filters worsens the performance resulting in a mean and standard deviation distance larger than 9.6 and 1.4 pixels, respectively. In addition, it is worth noting that both local speckle filters call for similar average performance (within 1 pixel), even though the Lee filter is less robust.

When dealing with the SAR scene of Fig. 3(b), local speckle filters result in the worst accuracy using either r and σ_{VH}^0 .

To further investigate the extraction accuracy, a statistical analysis that consists of discussing the accuracy achieved by different methods by quantiles is shown in Table II. It can be noted that when local filters are used, r always outperforms σ_{VH}^0 . When nonlocal filter is adopted, the difference between r and σ_{VH}^0 reduces significantly and both the metrics result in remarkable performance.

To discuss the accuracy of the coastline extraction methods against the incidence angle, the two Sentinel-1 scenes are processed. They were collected at an incidence angle of about 38° (very close to the RadarSAT-2 scenes) and 45° (i.e., a larger incidence angle). The SAR scenes are processed to obtain a pixel spacing of 13 m. Although the two Sentinel-1 SAR scenes are not timely collocated with the GPS ground truth (and, therefore, the

TABLE II
STATISTICS (QUANTILES) OF THE DISTANCE, IN PIXELS, BETWEEN THE DETECTED AND THE REFERENCE GPS COASTLINES

| SAR Scene | Metric | Speckle filter | | | | | | | | |
|------------|-----------------|----------------|------|------|-----|------|------|-----------|-----|-----|
| | | Boxcar | | | Lee | | | Non-local | | |
| | | 25% | 50% | 75% | 25% | 50% | 75% | 25% | 50% | 75% |
| Fig. 3 (a) | r | 8.9 | 10.2 | 11.1 | 8.2 | 10.1 | 12.3 | 5.6 | 6.4 | 7.1 |
| | σ_{VH}^0 | 9.7 | 10.5 | 11.3 | 8.1 | 9.7 | 11.3 | 5.7 | 6.3 | 7.1 |
| Fig. 3 (b) | r | 7.0 | 7.7 | 8.9 | 6.1 | 6.8 | 7.7 | 4.6 | 5.3 | 5.8 |
| | σ_{VH}^0 | 8.3 | 9.2 | 11.5 | 6.8 | 7.8 | 8.9 | 4.8 | 5.3 | 6.1 |

TABLE III
PERFORMANCE ANALYSIS WITH RESPECT TO THE INCIDENCE ANGLE. MEAN AND STANDARD DEVIATION DISTANCE (PIXELS) BETWEEN GPS MEASUREMENTS AND THE CORRESPONDING POINTS BELONGING TO THE COASTLINE EXTRACTED FROM THE TWO SENTINEL-1 SAR SCENES AT 38° AND 45° USING r AND σ_{VH}^0

| Incidence angle | Metric | Speckle filter | | | | | |
|-----------------|-----------------|----------------|------|------|------|-----------|------|
| | | Boxcar | | Lee | | Non-local | |
| | | Mean | Std | Mean | Std | Mean | Std |
| 38° | r | 1.56 | 0.89 | 1.21 | 0.96 | 0.69 | 0.58 |
| | σ_{VH}^0 | 1.11 | 0.72 | 0.99 | 0.74 | 0.94 | 0.76 |
| 45° | r | 0.98 | 0.72 | 0.77 | 0.52 | 0.55 | 0.36 |
| | σ_{VH}^0 | 1.31 | 0.97 | 1.06 | 0.68 | 0.91 | 0.56 |

results cannot be compared with the RadarSAT-2 SAR scenes), they can provide useful information on the effect of the incidence angle on the extraction accuracy.

Note that since different experimental conditions apply, no fair comparison with coastlines extracted from RadarSAT-2 SAR data can be performed. Experimental results are listed in Table III, where the mean accuracy measured in terms of mean \pm standard deviation distance (in pixels) with respect to GPS samples is shown. Even in this case, the nonlocal speckle filtering results in a better extraction accuracy if compared to local filters. When discussing the extraction accuracy against the incidence angle, one can note that both single- and dual-polarization metrics result in remarkable accuracy. In fact, the mean distance between the extracted coastlines and GPS samples is always smaller than 2 pixels. The mean accuracy slightly decreases when increasing the incidence angle for the single-polarization metric; while it increases when dealing with the dual-polarization one.

VI. CONCLUSION

In this study, multipolarization C-band SAR measurements are exploited for coastline extraction purposes over a challenging coastal environment that results in significant NRCS variability. State-of-the-art multipolarization coastline extraction metrics (either single- and dual-polarization), evaluated with different speckle filters (either local and nonlocal approaches), are considered. The analysis is quantitatively assessed by means of GPS samples collected over the Solway Firth coastal area, a test site characterized by different habitats as wetland, salt marshes, sand dunes, sand banks, mudflats, and intertidal flats. Full-polarimetric RadarSAT-2 and dual-polarimetric Sentinel-1 data are exploited to analyze the effects of the speckle filtering (local versus nonlocal) and the incidence angle on the coastline extraction accuracy.

Experimental results show that the joint combination of non-local speckle filters and dual-polarimetric information provides the best accuracy. In addition, larger incidence angles result in the best accuracy when the dual-polarization metric, augmented by a nonlocal filtering, is used.

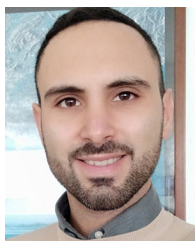
ACKNOWLEDGMENT

The authors would like to thank the Solway Firth Partnership and Natural Scotland for the logistical support during the fieldwork. They would like to thank to the Canadian Space Agency for providing the RadarSAT-2 SAR data under the Project ID 5440 entitled ‘‘Polarimetric change detection for wetlands’’ and ESA for providing the Sentinel-1 SAR data through the Copernicus Scientific Hub and also would like to thank the anonymous reviewers for their helpful comments and suggestions that allowed us to improve the manuscript.

REFERENCES

- [1] E. Doukakis, ‘‘Coastal vulnerability and risk parameters,’’ *Eur. Water*, vol. 51, no. 11/12, pp. 3–7, 2005.
- [2] J. Lee and E. Pottier, *Polarimetric Radar Imaging: From Basics to Applications*. Boca Raton, FL, USA: CRC Press, 2009.
- [3] J.-S. Lee and I. Jurkevich, ‘‘Coastline detection and tracing in SAR images,’’ *IEEE Trans. Geosci. Remote Sens.*, vol. 28, no. 4, pp. 662–668, Jul. 1990.
- [4] R. Pelich, M. Chini, R. Hostache, P. Matgen, and C. Lopez-Martinez, ‘‘Coastline detection based on Sentinel-1 time series for ship- and flood-monitoring applications,’’ *IEEE Geosci. Remote Sens. Lett.*, to be published, doi: 10.1109/LGRS.2020.3008011.
- [5] Y. Yu and S. T. Acton, ‘‘Automated delineation of coastline from polarimetric SAR imagery,’’ *Int. J. Remote Sens.*, vol. 25, no. 17, pp. 3423–3438, 2004.
- [6] M. Modava, G. Akbarizadeh, and M. Soroosh, ‘‘Hierarchical coastline detection in SAR images based on spectral-textural features and global local information,’’ *IET Radar, Sonar Navigation*, vol. 13, no. 12, pp. 2183–2195, 2019.
- [7] N. Baghdadi, R. Pedreros, N. Lenotre, T. Dewez, and M. Paganini, ‘‘Impact of polarization and incidence of the ASAR sensor on coastline mapping: Example of Gabon,’’ *Int. J. Remote Sens.*, vol. 28, no. 17, pp. 3841–3849, 2007.
- [8] W. M. Moon, G. Staples, D. Kim, S. Park, and K. Park, ‘‘Radarsat-2 and coastal applications: Surface wind, waterline, and intertidal flat roughness,’’ *Proc. IEEE*, vol. 98, no. 5, pp. 800–815, May 2010.
- [9] D. Kim, W. M. Moon, S. Park, J. Kim, and H. Lee, ‘‘Dependence of waterline mapping on radar frequency used for SAR images in intertidal areas,’’ *IEEE Geosci. Remote Sens. Lett.*, vol. 4, no. 2, pp. 269–273, Apr. 2007.
- [10] X. Ding, F. Nunziata, X. Li, and M. Migliaccio, ‘‘Performance analysis and validation of waterline extraction approaches using single- and dual-polarimetric SAR data,’’ *IEEE J. Sel. Topics Appl. Earth Observ. Remote Sens.*, vol. 8, no. 3, pp. 1019–1027, Mar. 2015.
- [11] E. Ferrentino, F. Nunziata, and M. Migliaccio, ‘‘Full-polarimetric SAR measurements for coastline extraction and coastal area classification,’’ *Int. J. Remote Sens.*, vol. 38, no. 23, pp. 7405–7421, 2017.

- [12] F. Nunziata, A. Buono, M. Migliaccio, and G. Benassai, "Dual-polarimetric C- and X-band SAR data for coastline extraction," *IEEE J. Sel. Topics Appl. Earth Observ. Remote Sens.*, vol. 9, no. 11, pp. 4921–4928, Nov. 2016.
- [13] J. Feng, L. Jiao, X. Zhang, M. Gong, and T. Sun, "Robust non-local fuzzy C-means algorithm with edge preservation for SAR image segmentation," *Signal Process.*, vol. 93, no. 2, pp. 487–499, 2013.
- [14] X. Xing, Q. Chen, S. Yang, and X. Liu, "Feature-based nonlocal polarimetric SAR filtering," *Remote Sens.*, vol. 9, no. 10, pp. 1043–1061, 2017.
- [15] M. Schmitt, G. Baier, and X. X. Zhu, "Potential of nonlocally filtered pursuit monostatic TanDEM-X data for coastline detection," *ISPRS J. Photogrammetry Remote Sens.*, vol. 148, pp. 130–141, 2019.
- [16] W. Wang *et al.*, "A fully polarimetric SAR imagery classification scheme for mud and sand flats in intertidal zones," *IEEE Trans. Geosci. Remote Sens.*, vol. 55, no. 3, pp. 1734–1742, Mar. 2017.
- [17] M. Gade, S. Melchionna, K. Stelzer, and J. Kohlus, "Multi-frequency SAR data help improving the monitoring of intertidal flats on the German North Sea coast," *Estuarine Coastal Shelf Sci.*, vol. 140, pp. 32–42, 2014.
- [18] S. Park, W. M. Moon, and D. Kim, "Estimation of surface roughness parameter in intertidal mudflat using airborne polarimetric SAR data," *IEEE Trans. Geosci. Remote Sens.*, vol. 47, no. 4, pp. 1022–1031, Apr. 2009.
- [19] J. H. Ryu, J. K. Choi, and Y. K. Lee, "Potential of remote sensing in management of tidal flats: A case study of thematic mapping in the Korean tidal flats," *Ocean Coastal Manag.*, vol. 102, pp. 458–470, 2014.
- [20] N. England, NCA profile: 06 solway basin (ne536), 2014. [Online]. Available: <http://publications.naturalengland.org.uk/publication/5276440824119296>
- [21] E. Ferrentino, F. Nunziata, A. Buono, A. Urciuoli, and M. Migliaccio, "Multipolarization time series of Sentinel-1 SAR imagery to analyze variations of reservoirs water body," *IEEE J. Sel. Topics Appl. Earth Observ. Remote Sens.*, vol. 13, pp. 840–846, 2020.
- [22] D. Di Luccio *et al.*, "Shoreline rotation analysis of embayed beaches by means of in situ and remote surveys," *Sustainability*, vol. 11, no. 3, pp. 725–744, 2019.
- [23] F. Nunziata, M. Migliaccio, X. Li, and X. Ding, "Coastline extraction using dual-polarimetric COSMO-SkyMed pingpong mode SAR data," *IEEE Geosci. Remote Sens. Lett.*, vol. 11, no. 1, pp. 104–108, Jan. 2014.
- [24] Z. Liu, F. Li, N. Li, R. Wang, and H. Zhang, "A novel region-merging approach for coastline extraction from Sentinel-1A IW mode SAR imagery," *IEEE Geosci. Remote Sens. Lett.*, vol. 13, no. 3, pp. 324–328, Mar. 2016.
- [25] M. Modava, G. Akbarizadeh, and M. Soroosh, "Integration of spectral histogram and level set for coastline detection in SAR images," *IEEE Trans. Aerosp. Electron. Syst.*, vol. 55, no. 2, pp. 810–819, Apr. 2019.
- [26] C. Deledalle, L. Denis, G. Poggi, F. Tupin, and L. Verdoliva, "Exploiting patch similarity for SAR image processing: The nonlocal paradigm," *IEEE Signal Process. Mag.*, vol. 31, no. 4, pp. 69–78, Jul. 2014.
- [27] A. Buades, B. Coll, and J. M. Morel, "A non-local algorithm for image denoising," in *Proc. IEEE Comput. Soc. Conf. Comput. Vis. Pattern Recognit.*, 2005, vol. 2, pp. 60–65.
- [28] A. Buades, B. Coll, and J. M. Morel, "A review of image denoising algorithms, with a new one," *J. Multiscale Model. Simul.*, vol. 4, no. 2, pp. 490–530, 2005.
- [29] F. Bachofer, G. Queneherve, T. Zwiener, M. Maerker, and V. Hochschild, "Comparative analysis of edge detection techniques for SAR images," *Eur. J. Remote Sens.*, vol. 49, no. 1, pp. 205–224, 2016.
- [30] M. M. Harvey and R. L. Allan, "The Solway Firth saltmarshes," *Scottish Geographical Mag.*, vol. 114, no. 1, pp. 42–45, 1998.
- [31] V. J. May and J. D. Hansom, "The Solway Firth saltmarshes," in *Coastal Geomorphology of Great Britain*. Peterborough, U.K.: Joint Nature Conservation Committee, ch. 10, vol. 28, 2003.



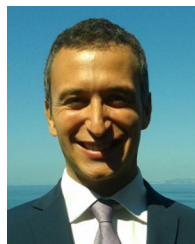
Emanuele Ferrentino (Student Member, IEEE) was born in Cattolica, Italy, in 1984. He received the B.Sc. and M.Sc. degrees in telecommunication engineering from the Universit di Napoli "Parthenope", Napoli, Italy, in 2010 and 2014, respectively. He received the Ph.D. degree in information engineering from the Universit degli Studi di Napoli "Parthenope," Napoli, Italy, in 2019.

Since 2019, he has been a Postdoctoral Research Fellow with the Universit degli Studi di Napoli "Parthenope." His research interests include electromagnetic modeling, polarimetric SAR data analysis, and remote sensing land and marine applications (earthquake damage assessment, target detection, coastline extraction, and classification).



Andrea Buono (Member, IEEE) was born in Napoli, Italy, in 1984. He received the B.Sc. and M.Sc. degrees in telecommunication engineering from the Universit di Napoli "Parthenope", Napoli, Italy, in 2010 and 2013, respectively. He received the Ph.D. degree in information engineering from the Universit di Napoli "Parthenope", Napoli, Italy, in 2017.

Since 2018 he has been an Assistant Professor with Universit di Napoli "Parthenope". His main research activities deals with applied electromagnetics, including electromagnetic modeling, polarimetry, ocean, and coastal area applications.



Ferdinando Nunziata (Senior Member, IEEE) was born in Avellino, Italy, in 1982. He received the B.Sc., M.Sc., and Ph.D. degrees in telecommunication engineering from the Universit di Napoli Parthenope, Napoli, Italy, in 2003, 2005, and 2008, respectively.

Since 2019, he has been an Associate Professor with Universit di Napoli "Parthenope". His main research interests include applied electromagnetics, i.e., sea surface scattering, radar polarimetry, SAR sea oil slick and metallic target monitoring, spatial resolution enhancement techniques, and global navigation

satellite system (GNSS)-R.



Armando Marino (Member, IEEE) received the M.Sc. degree in telecommunication engineering from the Universit di Napoli "Federico II," Naples, Italy, in 2006, and the Ph.D. degree in polSAR interferometry from the School of Geosciences, University of Edinburgh, Edinburgh, U.K., in 2011. From 2011 to 2015, he was a Postdoctoral Researcher and a Lecturer with Institute of Environmental Engineering, ETH Zurich, Zrich, Switzerland. Since 2015, he has been a Lecturer with the School of Engineering and Innovation, Open University, Milton Keynes, U.K. Since 2018,

he has been a Senior Lecturer (Assistant Professor) with the Faculty of Natural Sciences, University of Stirling, Stirling, U.K.



Maurizio Migliaccio (Fellow, IEEE) was born in Napoli, Italy, in 1962. He received the Laurea degree (Hons.) in electronic engineering from the Universit di Napoli Federico II, Napoli, Italy, in 1987.

He is currently a Full Professor of Electromagnetics with the Universit di Napoli Parthenope, Napoli, Italy. His current scientific interests include remote sensing for marine and coastal applications, polarimetry, inverse problem for resolution enhancement, and reverberating chambers.